



A discontinuous finite element solution of the Boltzmann kinetic equation in collisionless and BGK forms for macroscopic gas flows

Ben Evans*, Ken Morgan, Oubay Hassan

Civil & Computational Engineering Centre, Swansea University, SA2 8PP, UK

ARTICLE INFO

Article history:

Received 22 June 2009

Received in revised form 29 June 2010

Accepted 6 July 2010

Available online 25 July 2010

Keywords:

Taylor–Galerkin

Discontinuous

Boltzmann

BGK

Hypersonic

ABSTRACT

In this paper, an alternative approach to the traditional continuum analysis of flow problems is presented. The traditional methods, that have been popular with the CFD community in recent times, include potential flow, Euler and Navier–Stokes solvers. The method presented here involves solving the governing equation of the molecular gas dynamics that underlies the macroscopic behaviour described by the macroscopic governing equations. The equation solved is the Boltzmann kinetic equation in its simplified collisionless and BGK forms. The algorithm used is a discontinuous Taylor–Galerkin type and it is applied to the 2D problems of a highly rarefied gas expanding into a vacuum, flow over a vertical plate, rarefied hypersonic flow over a double ellipse, and subsonic and transonic flow over an aerofoil. The benefit of this type of solver is that it is not restricted to continuum regime (low Knudsen number) problems. However, it is a computationally expensive technique.

© 2010 Elsevier Inc. All rights reserved.

1. Introduction

1.1. The Boltzmann equation

In recent decades, the CFD community has largely focused on the solution and application of the Euler and Navier–Stokes equation systems in finding solutions to fluid flow problems [15–17,23,24]. Solution of these equations requires the assumption that the fluid in question can be regarded as continuous. This assumption allows us to express shear stresses and heat flux in terms of the lower order macroscopic variables such as pressure and temperature and thus close the equation set.

Continuum validity can be expressed in terms of the Knudsen number (Kn), which is the ratio of the mean free molecular path, the average distance of molecular travel between collisions, to some typical length scale of the flow, and is a measure of the degree of rarefaction of a gas. It has been shown [18] that above $Kn \approx 0.1$, we enter the transition regime beyond which the continuum assumption breaks down. Once we reach this limit, we should no longer solve continuum equations. Instead, we should solve the Boltzmann equation, from which the continuum equations can be derived [19].

The Boltzmann equation considers a gas at the molecular level. It has a single dependant variable, compared with several dependant variables in the Euler/Navier–Stokes systems. However, this variable, known as the *distribution function*, f , is defined over physical space and velocity space (and time), i.e. $f = f(\mathbf{r}, \mathbf{c}, t)$, where \mathbf{r} is a position vector in physical space and \mathbf{c} is a position vector in velocity space. The distribution function is a probability function, giving a measure of the probability that a molecule exists at a given location in physical space travelling with a given velocity (at any given time). The solution is thus said to be defined over *phase space*. This is the combination of real physical space (p -space), which will vary depending on the

* Corresponding author. Tel.: +44 1792602129.

E-mail address: b.j.evans@swansea.ac.uk (B. Evans).

problem, and velocity space (*v*-space), which in principle, is unbounded. There are a variety of forms for the distribution function. The definition used throughout this paper is

$$dN = f(\mathbf{c}, \mathbf{r}, t) d\mathbf{c} d\mathbf{r}, \tag{1}$$

with *dN* representing the number of molecules in the phase space element *dcdr*. In cartesian coordinates, this definition implies that *dN* is the number of molecules with spatial coordinates lying in the range *x* to *x* + *dx*, *y* to *y* + *dy*, *z* to *z* + *dz* where *dx*, *dy*, *dz* are small increments in *x*, *y*, *z*, and with velocity components lying in the range *u* to *u* + *du*, *v* to *v* + *dv*, *w* to *w* + *dw* where *du*, *dv*, *dw* are small increments in *u*, *v*, *w*. Integrating over all phase space gives the total number of molecules in the system, *N*.

The class of a molecule is defined by its velocity state, i.e. all molecules travelling with with velocity **c** to **c** + **dc** are said to be class **c** molecules. Applying molecular class conservation to an appropriately defined control volume in *p*-space, Δ**r** (this is equivalent to conservation of all molecules in phase space Δ**r**Δ**c**) leads to the Boltzmann equation of molecular gas dynamics

$$\frac{\partial(nf)}{\partial t} + \mathbf{c} \frac{\partial(nf)}{\partial \mathbf{r}} = \frac{1}{Kn} Q(f, f), \tag{2}$$

where *n* is the molecular number density of the gas and *Q(f,f)* is the term accounting for the collision of molecules [1]. It is beyond the scope of this paper to provide a more formal derivation of the Boltzmann kinetic equation but for more details on thorough mathematical derivations please refer to [1,2,4]. The term *Q(f,f)* is a five-fold integral (in 3*p*-space dimensions) and is the source of much of the difficulty in solving this non-linear integro–differential equation. The Boltzmann equation may also be derived from the Liouville equation ([3–5]) and this method is the most mathematically rigorous in terms of determining the limits of validity of the equation.

By making the continuum assumptions, it is possible to derive the Euler and Navier–Stokes equations via a process known as ‘taking moments’ of the equation [1]. If the Boltzmann equation is tractable, and the distribution function can be determined across phase space, the more familiar macroscopic variables; density, velocity, pressure, temperature may be determined by taking moments of the distribution function. This is detailed in Section 1.2.

If the Knudsen number is sufficiently large (*Kn* ≫ 1), we can ignore the term on the right-hand side of Eq. (2). This is due to collisions between molecules becoming insignificant in terms of class conservation compared with molecular convection. Setting the right-hand side to zero, results in the significantly simplified collisionless Boltzmann equation,

$$\frac{\partial(nf)}{\partial t} + \mathbf{c} \frac{\partial(nf)}{\partial \mathbf{r}} = 0. \tag{3}$$

An expression for the distribution function of a gas in thermodynamic equilibrium was established late in the 19th by Maxwell [6,13], and later confirmed by Boltzmann himself. This has now become known as the Maxwell–Boltzmann equilibrium distribution function or simply the Maxwellian distribution function. The form of this distribution function is,

$$f_0 = \left(\frac{\beta^3}{\pi^{3/2}} \right) \exp \left(-\beta^2 (\mathbf{c} - \mathbf{c}_0)^2 \right), \tag{4}$$

in 3-dimensions, where **c**₀ is the bulk velocity of the flow and β = (2*RT*)^{−1/2} = √*m*/(2*kT*). *R* is the universal gas constant, *T* is the gas temperature measured in Kelvin, *m* is the molecular mass and *k* is the Boltzmann constant (1.380 650524 × 10^{−23} J/K).

Simplified versions of the full Boltzmann equation exist in which the right-hand side term is modelled rather than expressed explicitly in its integral form. The best known model equation due to Bhatnager, Gross and Krook [7] is called the BGK equation. In a non-equilibrium gas the assumption is made that the effect of molecular collisions is to force the distribution function back to equilibrium. The integrals in the term *Q(f,f)* on the right-hand side of Eq. (2) mathematically describe this process and can, therefore, be replaced by the term *v(c)((nf₀) − (nf))*, where *n* again is the molecular number density, *v(r,t)* is the molecular collision frequency and *f*₀ is the local Maxwellian equilibrium distribution function. The Boltzmann–BGK equation may therefore be written as

$$\frac{\partial(nf)}{\partial t} + \mathbf{c} \frac{\partial(nf)}{\partial \mathbf{r}} = v(\mathbf{r}, t)((nf_0) - (nf)). \tag{5}$$

The inclusion of the equilibrium distribution function means that the BGK equation is still a non-linear integro–differential equation, because *f*₀ is a function of the stream velocity, **c**₀, and the temperature, *T*, which are obtained by taking integrals over *f* (see Section 1.2). However, computationally, the BGK term is significantly less demanding than the full right-hand side term.

1.2. Moments of the distribution function

The form of the distribution function at any point in physical space is not particularly useful in itself, but knowledge of the distribution function allows us to calculate more familiar gas properties, such as density, ρ, temperature, *T*, pressure, *p*, and bulk velocity, **v**, by taking moments of the distribution function.

At each point in physical space, the mean value of any molecular quantity, Q , is defined as

$$\bar{Q} = \int_{-\infty}^{\infty} Qf(\mathbf{c})d\mathbf{c}. \tag{6}$$

By setting Q to the appropriate molecular quantity, we can obtain the macroscopic properties as follows;

- density ρ : $Q = nm$ where m is the molecular mass
- bulk velocity \mathbf{v} : $Q = \mathbf{c}$
- static pressure \mathbf{p} : $Q = nm\overline{c_i c_j}$ where $c'_i = c_i - v_i$ (thermal/peculiar velocity)

This definition of static pressure is clearly a vector quantity and this is a true characteristic of a non-equilibrium gas. We are more accustomed to dealing with pressure as a scalar and the static pressures specified in this work will be taken as the mean of the Cartesian components.

We simply use the definition of kinetic temperature,

$$T_k = \frac{p}{R\rho}, \tag{7}$$

where p is the mean value of the pressure vector components as described above.

2. The solution approach

2.1. Discretisation of the solution domains

As the primary unknown in the problem is defined across both *physical space* and *velocity space*, we must adopt a suitable discretisation procedure for both domains. In this work we restrict ourselves to two dimensional problems. The physical space domain, Ω_r is discretised into an unstructured assembly of discontinuous, linear, triangular elements with nodes at the vertices as shown in Fig. 1. Although at this stage, only relatively simple geometry problems will be considered, the choice of an unstructured mesh approach allows for straightforward extension to problems involving complex geometries in future work.

The corresponding two dimensional v -space domain, Ω_c , depicted in Fig. 2, is in principle, infinite in extent. However, we must place a finite limit on the radial extent of the domain, which in real, physical terms means placing a limit on the maximum possible speed of a molecule. In this way, we are making the assumption that any molecules travelling faster than this critical speed have negligible impact on the bulk flow properties. Gauging where this limit should be placed is critical for ensuring a balance between accurate results and computational efficiency. A standard rule of thumb for the limit is that the maximum speed in v -space should be at least several times the mean thermal (or peculiar) molecular velocity [1]. The thermal velocity is defined as the component of molecular velocity relative to the fluid velocity. An order of magnitude estimation for the value of the mean thermal molecular velocity can be calculated using some simple kinetic theory results. The moment calculation for the non-equilibrium static pressure in a given direction is

$$\mathbf{p} = \int_{-\infty}^{\infty} nm\overline{c_i c_j}f(\mathbf{c})d\mathbf{c} \tag{8}$$

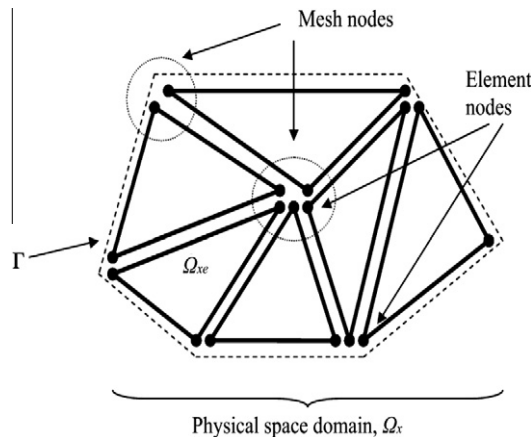


Fig. 1. Discretisation of physical space.

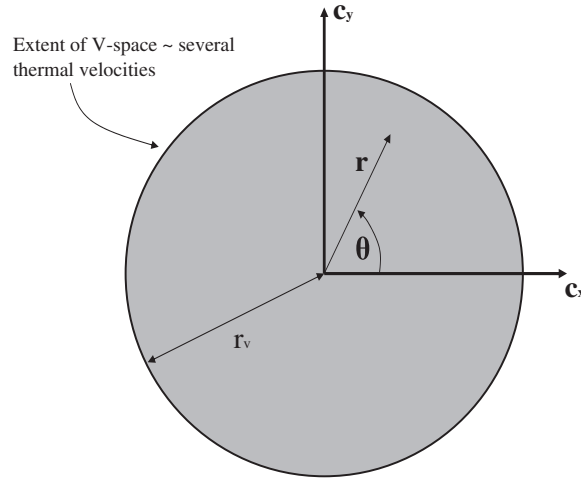


Fig. 2. Velocity space domain.

and, taking an average over three spatial dimensions, it follows that

$$p = 1/3\rho\bar{c}^2. \tag{9}$$

Combining this result with Eq. (7), it is apparent that the rms thermal molecular velocity may be written as

$$\sqrt{\bar{c}^2} = \sqrt{3RT_k}. \tag{10}$$

As the v -space domain contains no internal geometries, it can be discretised as a single high order (spectral) element. This is advantageous for efficient integration over the domain. However, in order to apply a high order discretisation, it is convenient to map the domain from polar coordinates in real space as shown in Fig. 2 into a standard quadrilateral element in the (η, ζ) plane as shown in Fig. 3. The mapping is achieved using the transformation

$$\begin{aligned} \eta &= \frac{2r}{r_v} - 1, \\ \zeta &= \frac{\theta}{\pi}. \end{aligned} \tag{11}$$

where (r, θ) are polar coordinates in real v -space and r_v is the radius of the v -space domain, i.e. the maximum molecular speed. A high order quadrature method is then applied to the element. In the η direction, a Lobatto quadrature is applied whereas in the ζ direction a constant spacing/constant weighting discretisation is applied. This results in a rotationally symmetric distribution of sampling points with no preferred radial direction, when the points are mapped back into real space.

The coordinates of the quadrature points and the associated weightings in the (η, ζ) plane are shown in Fig. 4 for a (20×20) discretisation. If these points are then mapped back into real space, the (u, v) plane, the corresponding coordinates and weights are as shown in Fig. 5.

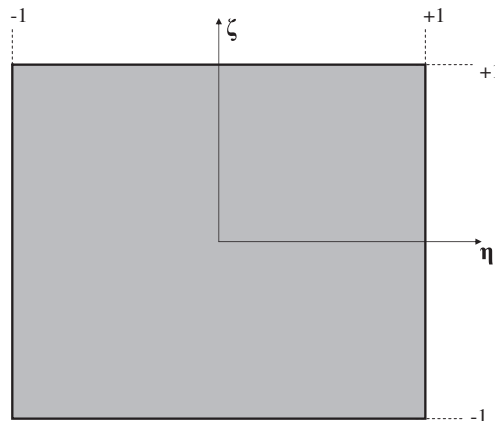


Fig. 3. A standard quadrilateral element in the (η, ζ) plane.

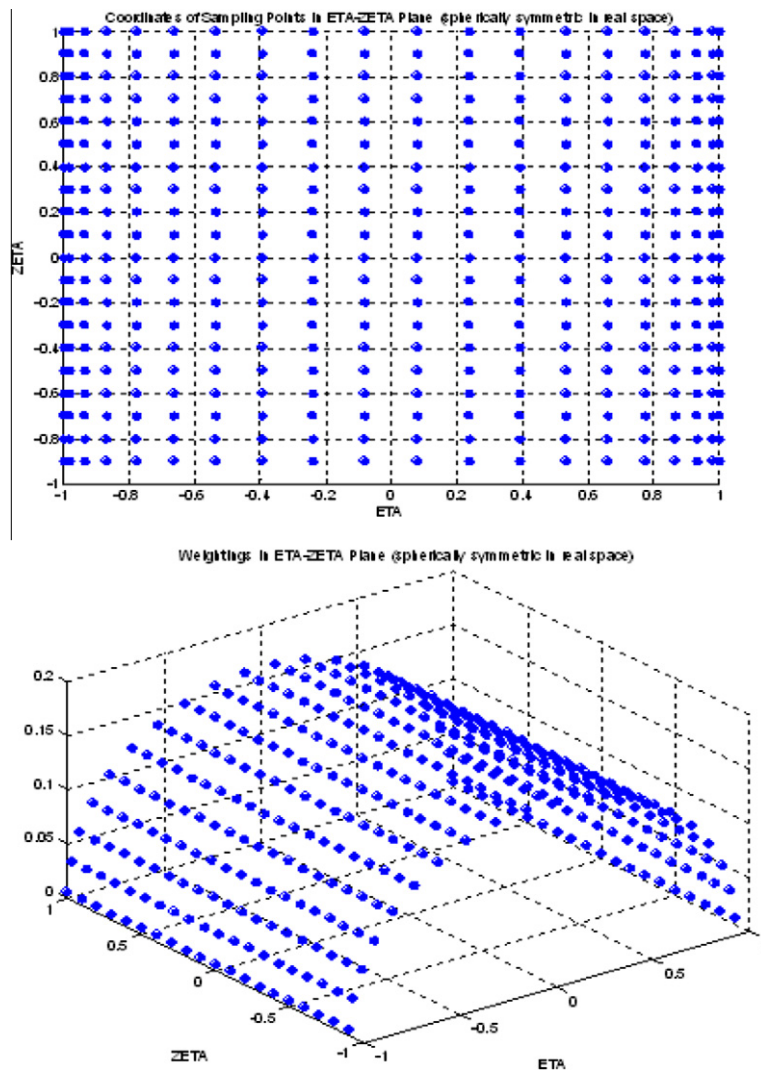


Fig. 4. Quadrature coordinates and weights in the (η, ζ) plane.

One of the dangers of approximating a function using spectral methods is the Runge phenomenon [12]. However, it is the accuracy of the integrals of the distribution function over v -space that is of concern here. This is because, ultimately, it is the macroscopic variables that are of interest which are computed by taking moments of the distribution function. Testing of this method for typical forms of the distribution function showed that this spectral approach was perfectly capable of accurately performing the necessary integrals. A rigorous mathematical analysis of quadrature methods for circular domains is contained in [11].

2.2. Nomenclature

Since the molecular number density, n , and the distribution function, f , always appear together in the Boltzmann–BGK equation, we can solve for the unknown variable nf . There is no computational advantage in separating these variables since they appear together in the computation of the moment integrals at the post-processing stage. We must be able to specify this discretised unknown in terms of space, velocity and time. Therefore, we will write $(nf)_{r,c}^m$ meaning the value of nf at time-step m , spatial coordinate \mathbf{r} and velocity coordinate \mathbf{c} . This subscript/superscript notation will also be applied to other appropriate variables.

2.3. Application of the finite element method

Upon consideration of Eq. (5), it is apparent that the form of this equation is not dissimilar to the simple scalar convection equation with a source term on the right-hand side. There is, however, one critical difference, that in (5) the dependant

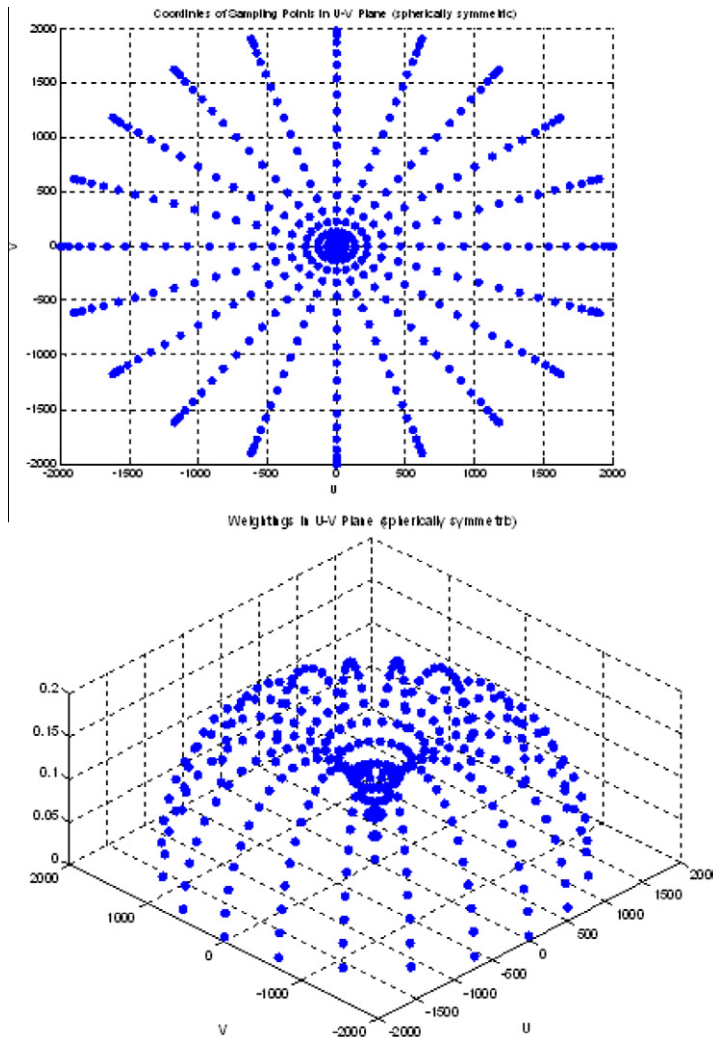


Fig. 5. Quadrature coordinates and weights in the (u, v) plane.

variable, nf , is a function not just of space and time, but also of velocity, \mathbf{c} . Upon consideration we find that if we fix our position in v -space, i.e. hold \mathbf{c} constant, then the form of the Boltzmann–BGK equation is identical to that of the scalar convection equation with source term. This allows us to develop a Boltzmann–BGK solver based on a standard discontinuous Taylor–Galerkin ([8,9]) algorithm for the scalar convection equation. This is achieved by looping over the sampling points in v -space and applying an adapted scalar convection algorithm at each v -space sampling point independently. The convection velocity used is given by the coordinate of the v -space node in question. A Galerkin weighted residual method is used together with the approximation

$$(nf)_i^{m+\frac{1}{2}} = (nf)_i^m + \left(\frac{\Delta t}{2}\right) Q^m - \frac{\Delta t}{2} c_i \frac{\partial (nf)_j}{\partial r_j} \Big|_i^m, \tag{12}$$

to obtain the increment $\Delta(nf)$ in a two-step manner. In Eq. (12), Q is computed as $Q = v(\mathbf{r}, t)((nf_0) - (nf))$ with f_0 representing the Maxwellian equilibrium distribution function, given in Eq. (4), modified to its two dimensional form, $f_0(\mathbf{c}) = (\beta^2/\pi) \exp(-\beta^2(\mathbf{c} - \mathbf{c}_0)^2)$ and v is the molecular collision frequency determined as

$$v(\mathbf{r}, t) = \int_{-\infty}^{+\infty} \sigma_T |\mathbf{c} - \mathbf{c}_1| f d\mathbf{c}_1, \tag{13}$$

where σ_T is the total collision cross section [1]. If we make the assumption of hard sphere molecules, we obtain the simplest possible expression for the total collision cross section, $\sigma_T = \pi d^2$, where d is the molecular diameter.

Of course, in the special case when it is the collisionless Boltzmann Eq. (3) that is being solved, we simply set the collision term, Q to zero in this application method.

2.3.1. First step

A piecewise-constant increment $\Delta(nf)_{re,c}$ is computed on each physical space element according to

$$\Delta(nf)_{re,c} = \frac{\Delta t}{2} \sum Q_{k,c}^m N_k - \frac{\Delta t}{2} F_{ik}^m \frac{\partial N_k}{\partial r_i} \Big|_{re,c}, \tag{14}$$

where the summation k extends over the three nodes of element re , Δt is the global timestep governed by the Courant stability condition

$$\Delta t < \frac{0.5 h_{min}}{|\mathbf{v}|_{max}}, \tag{15}$$

with h_{min} representing some minimum characteristic element size in the physical space mesh and $|\mathbf{v}|_{max}$ denoting the maximum velocity in the velocity space mesh. Here, N_k is the standard, piecewise, linear finite element shape function associated with node k in physical space and

$$F_{ik,c}^m = F_i((nf)_{k,c}^m) = \mathbf{c}(nf)_{k,c}^m. \tag{16}$$

The element fluxes at the half-timestep are then approximated by the piecewise linear discontinuous representation

$$F_i^{m+\frac{1}{2}} \Big|_{re,c} = F_i((nf)_{k,c}^m + \Delta(nf)_{re,c}) N_k. \tag{17}$$

2.3.2. Second step

A piecewise-linear approximation for $\Delta(nf)$ on each physical space element is assumed which is discontinuous at the element edges. The element nodal values of the solution increment over the complete timestep are determined according to

$$M_L]_{re} \Delta(nf)_{k,c} = \Delta t M_L]_{re} Q^{m+\frac{1}{2}} + \Delta t \int_{\Gamma_{re}} F_{n,c}^{m+\frac{1}{2}} N_k d\Gamma_{re} - \Delta t \int_{\Omega_{re}} F_{ik,c}^{m+\frac{1}{2}} \frac{\partial N_k}{\partial r_i} d\Omega_{re,c} \tag{18}$$

where $M_L]_{re}$ is the standard, lumped, 3×3 physical space element mass matrix, $F_{n,c}^{m+\frac{1}{2}}$ denotes the normal component of the upstream flux at the physical space element edges for a velocity of \mathbf{c} (this inter-element flux will be dependant on boundary conditions if the edge is at a domain boundary), Γ_{re} is the physical space element boundary and Ω_{re} is the physical space element domain.

For inter-element edges, the direction of the flux across the edge must be calculated based on the convection velocity. The convection velocity is determined by the v -space mesh node under consideration. If the flux is ‘into the element’, the integral in the first term on the RHS of (18) is given a value based on the corresponding upstream element edge flux, i.e. with reference to Fig. 6, $F_{n,c}^{m+\frac{1}{2}} = \frac{1}{2} \mathbf{c} \cdot \mathbf{n} ((nf)_1^{m+\frac{1}{2}} + (nf)_2^{m+\frac{1}{2}})$. If the flux is ‘out of the element’, the same term is given a negative value based on the normal edge flux at that edge in the element. This ensures the local conservativeness of the scheme, since the fluxes of the distribution function are transferred directly from one element to the next.

In the BGK formulation shown here, the term ν is regarded as a collision frequency term and governs the rate at which the distribution function is restored to equilibrium. The form of the BGK collision term is such that the distribution function will be restored to equilibrium in a timescale,

$$\tau = O\left(\frac{1}{\nu}\right). \tag{19}$$

This places a further restriction on the allowable timestep size

$$\Delta t < \frac{1}{\nu}. \tag{20}$$

in addition to the Courant condition, Eq. (15).

We now have two limits on the allowable timestep size. The Courant limit, condition (15), is fixed by the mesh geometries, whilst the BGK limit, condition (20), varies as the solution proceeds through time. This is due to its dependance on the

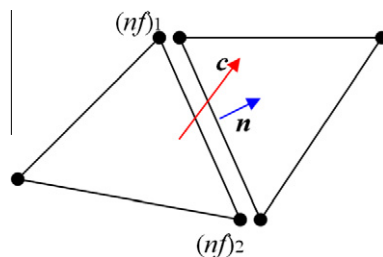


Fig. 6. Construction of the inter-element flux.

molecular collision frequency which, in turn, is dependant on pressure and temperature. This has the obvious effect of increasing the computational demand as density, and hence, pressure increase, since the timestep size must reduce.

2.4. Boundary conditions

Note that there are a range of potential approaches to dealing with boundary conditions in solution of the Boltzmann equation detailed in the literature ([19,2,20]). In this work, application of the boundary conditions in the algorithm is achieved by an appropriate modelling of $F_{n,c}^{m+\frac{1}{2}}$ in the first term on the right-hand side of Eq. (18).

Essentially, three types of boundary need to be considered; inflow, outflow and wall.

2.4.1. Inflow boundary condition

If the assumption is made that the gas flow entering the domain is in thermodynamic equilibrium, and we know the macroscopic properties of the gas, i.e. density, bulk velocity, pressure, temperature, then we are in a position to be able to construct the Maxwellian distribution function for the inflow.

For element edges at an inflow boundary, calculation of the inter-element flux will depend upon whether the molecular velocity is in a direction that is ‘into’ the element ($\mathbf{c}\cdot\mathbf{n} < 0$), as in the top element in Fig. 7, or the molecular velocity is in a direction that is ‘out of’ the element ($\mathbf{c}\cdot\mathbf{n} > 0$) as in the bottom element in Fig. 7.

In the first case, the molecular velocity is directed into the element, and the inter-element flux is constructed as

$$F_{n,c}^{m+\frac{1}{2}} = \mathbf{c}\cdot\mathbf{n} \left(\frac{\beta^2}{\pi} \right) \exp(-\beta^2(\mathbf{c} - \mathbf{c}_0)). \tag{21}$$

$(\beta^2/\pi) \exp(-\beta^2(\mathbf{c} - \mathbf{c}_0))$ is the Maxwellian distribution function in two dimensions.

If the molecular velocity is directed out of the element, the inter-element flux is constructed as

$$F_{n,c}^{m+\frac{1}{2}} = \frac{1}{2} \mathbf{c}\cdot\mathbf{n} \left((nf)_1^{m+\frac{1}{2}} + (nf)_2^{m+\frac{1}{2}} \right). \tag{22}$$

2.4.2. Outflow boundary condition

If a domain boundary is an outflow based on the bulk flow at that boundary, the assumption is made that the gradient of macroscopic variables is zero perpendicular to the boundary and, therefore, that the gradient of the underlying distribution function is zero perpendicular to the boundary. This means that it is important to carefully select the position of the boundary of the domain of the problem, so that this condition would be met physically in the real system. This is in order to avoid any unwanted reflection effects resulting from application of the boundary condition. For example, in the case of flow from left to right over an aerofoil, the right-hand, outflow boundary must be placed sufficiently far downstream for any gradients in the solution to be zero or sufficiently far downstream, so that reflection effects will not affect the region of interest.

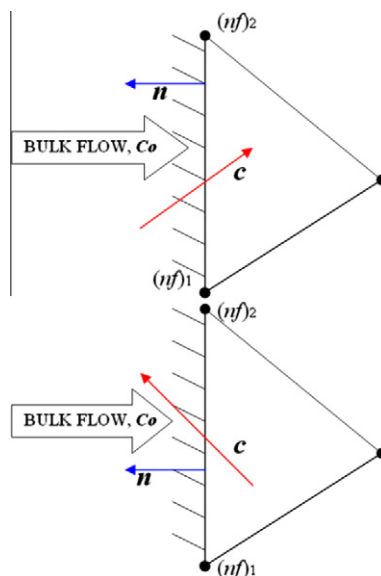


Fig. 7. Element edges at an inflow boundary.

For element edges at an outflow boundary, the construction of the inter-element flux is independent of the direction of the molecular velocity, i.e. it is independent of $\mathbf{c}\cdot\mathbf{n}$. The inter-element flux is constructed as (See Fig. 8)

$$F_{n,c}^{m+\frac{1}{2}} = \frac{1}{2} \mathbf{c}\cdot\mathbf{n} \left((nf)_1^{m+\frac{1}{2}} + (nf)_2^{m+\frac{1}{2}} \right) \tag{23}$$

and can, therefore, take on a positive or negative value.

2.4.3. Wall boundary condition

At a wall, the condition that must be enforced is zero mass flux across the boundary. In a kinetic theory description, this is expressed as

$$\int_{\Gamma_r} \int_{-\infty}^{+\infty} F_{n,c} d\mathbf{c} d\Gamma_r = 0, \tag{24}$$

where $F_{n,c} = (\mathbf{c}\cdot\mathbf{n})f(\mathbf{c}, \mathbf{r}, t)$ and Γ_r is the p -space domain boundary. This condition is ensured by an appropriate modelling of molecular collisions with the wall. We make the assumption that a certain fraction, α , of molecules are absorbed by the wall and remitted in equilibrium with wall, i.e. they are reflected back into the domain with a Maxwellian distribution based on the wall temperature. This is termed diffuse reflection. The remaining fraction, $(1 - \alpha)$, are not absorbed by the wall and simply reflect directly back into the domain. This is termed specular reflection. These two models, for the interaction of a flux of molecules with a solid surface, was first suggested by Maxwell [6]. The term α is known as the ‘absorption coefficient’. The distribution function of the net reflected flux of molecules is, therefore, constructed as

$$f(\mathbf{c}, \mathbf{r}, t) = (1 - \alpha)Rf(\mathbf{c}, \mathbf{r}, t) + \alpha Mf(\mathbf{c}, \mathbf{r}, t), \quad \text{for } \mathbf{c}\cdot\mathbf{n} \leq 0, \tag{25}$$

where

$$Rf(\mathbf{c}, \mathbf{r}, t) = f(\mathbf{c} - 2\mathbf{n}(\mathbf{n}\cdot\mathbf{c}), \mathbf{r}, t), \tag{26}$$

$$Mf(\mathbf{c}, \mathbf{r}, t) = \eta(\mathbf{r}, t)M_w(\mathbf{c}) \tag{27}$$

and \mathbf{n} is the outward facing unit normal at the wall, as shown in Fig. 9. If T_w is the wall temperature and R is the gas constant, then M_w is determined as

$$M_w = \exp\left(-\frac{c^2}{2RT_w}\right). \tag{28}$$

The parameter η is used to enforce the condition in Eq. (24) i.e. it is used to ensure conservation of mass at the the wall, which implies that

$$\eta(\mathbf{r}, t) = \frac{\int_{\mathbf{c}\cdot\mathbf{n}(\mathbf{r}) > 0} f(\mathbf{c}, \mathbf{r}, t) |\mathbf{c}\cdot\mathbf{n}(\mathbf{x})| d\mathbf{c}}{\int_{\mathbf{c}\cdot\mathbf{n}(\mathbf{r}) \leq 0} M_w(\mathbf{c}) |\mathbf{c}\cdot\mathbf{n}(\mathbf{x})| d\mathbf{c}}. \tag{29}$$

A technique similar to this has been applied by Pareschi and Trazzi [10] to a time relaxed Monte Carlo procedure for solution of the Boltzmann equation.

For molecular velocities towards the wall ($\mathbf{c}\cdot\mathbf{n} > 0$), as in the left-hand element in Fig. 10, the inter-element flux is constructed as

$$F_{n,c}^{m+\frac{1}{2}} = \frac{1}{2} \mathbf{c}\cdot\mathbf{n} \left((nf)_1^{m+\frac{1}{2}} + (nf)_2^{m+\frac{1}{2}} \right). \tag{30}$$

At a wall boundary, the construction of the inter-element flux will depend on the direction of the molecular velocity. For molecular velocities away from the wall ($\mathbf{c}\cdot\mathbf{n} < 0$), as in the right-hand element in Fig. 10, the inter-element flux is constructed based on the reflected distribution function defined by Eq. (25), so that

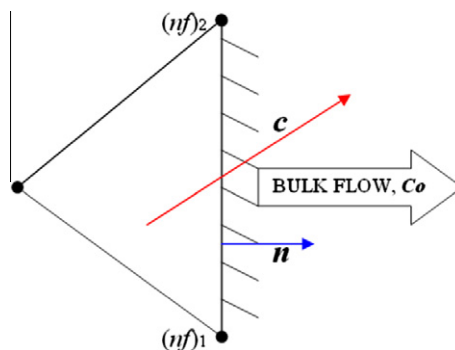


Fig. 8. Element edge at an outflow boundary.

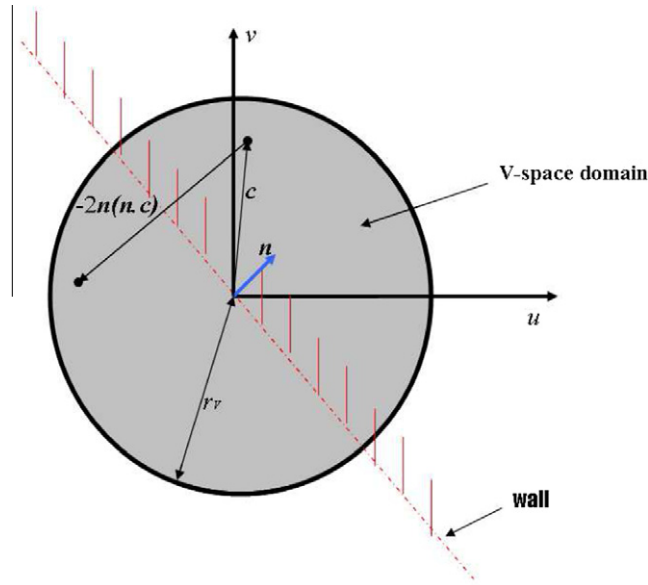


Fig. 9. Coordinate transformation in v -space under specular reflection.

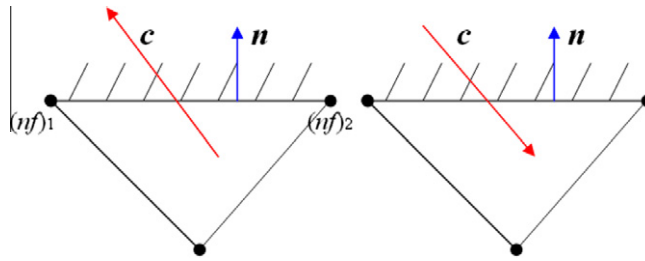


Fig. 10. Element edges at a wall boundary.

$$F_{n,c}^{m+\frac{1}{2}} = \mathbf{c} \cdot \mathbf{n} \left((1 - \alpha) R f^{m+\frac{1}{2}}(\mathbf{c}, \mathbf{r}, t) + \alpha M f^{m+\frac{1}{2}}(\mathbf{c}, \mathbf{r}, t) \right). \tag{31}$$

Here, α is the absorption coefficient and

$$R f^{m+\frac{1}{2}}(\mathbf{c}, \mathbf{r}, t) = f^{m+\frac{1}{2}}(\mathbf{c} - 2\mathbf{n}(\mathbf{n} \cdot \mathbf{c}), \mathbf{r}, t), \tag{32}$$

$$M f^{m+\frac{1}{2}}(\mathbf{c}, \mathbf{r}, t) = \eta^{m+\frac{1}{2}}(\mathbf{r}, t) M_w(\mathbf{c}). \tag{33}$$

If T_w is the wall temperature and R is the gas constant, then M_w is determined as

$$M_w = \exp\left(-\frac{c^2}{2RT_w}\right) \tag{34}$$

and

$$\eta^{m+\frac{1}{2}}(\mathbf{r}, t) = \frac{\int_{\mathbf{c} \cdot \mathbf{n}(\mathbf{r}) > 0} f^{m+\frac{1}{2}}(\mathbf{c}, \mathbf{r}, t) |\mathbf{c} \cdot \mathbf{n}(\mathbf{x})| d\mathbf{c}}{\int_{\mathbf{c} \cdot \mathbf{n}(\mathbf{r}) \leq 0} M_w(\mathbf{c}) |\mathbf{c} \cdot \mathbf{n}(\mathbf{x})| d\mathbf{c}}. \tag{35}$$

As the approach for spectral v -space discretisation outlined in Section 2.1 is rotationally symmetric about the origin, in terms of the locations of the sampling points, it is straightforward to perform integrals over half of the v -space domain. The procedure for performing integrals over the full v -space is detailed in the following section. The modification necessary here to integrate over half of the v -space is to only include sampling points for which $\mathbf{c} \cdot \mathbf{n} > 0$. This allows the determination of the integral in the numerator on the right-hand side of Eq. (35). The integral in the denominator can be determined using an analytical approach.

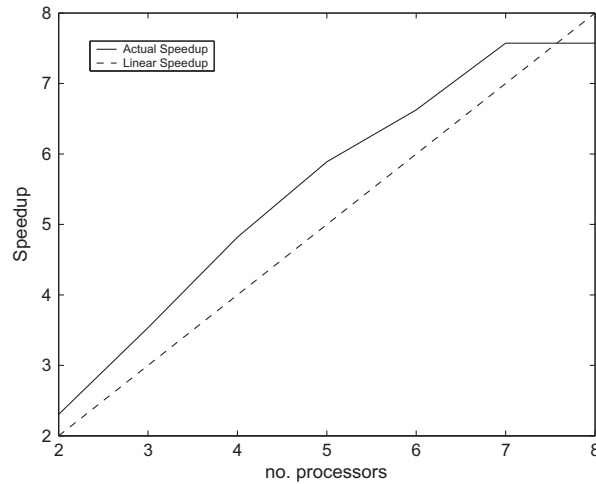


Fig. 11. Parallelisation speedup.

2.5. Initial condition

Since the solution field in the entire domain is relaxed explicitly to a steady-state solution, an appropriate initial condition must be applied at $t = 0$ across the entire phase space domain. A Maxwellian distribution function based upon the prescribed free-stream conditions of the problem is chosen, as in Eq. (21), modified for this two dimensional treatment.

2.6. Regaining the macroscopic variables

Regaining the macroscopic variables from the distribution function solution over phase space requires computation of the moment integrals detailed in Section 1.2. We must compute these integrals by transforming the coordinate system from the real v -space coordinates to the (η, ζ) plane. Moving from Cartesian to polar coordinates gives us

$$\bar{Q} = \int_{-1}^{+1} \int_{-1}^{+1} Qf(\eta, \zeta) \frac{\pi r_v^2}{4} (\eta + 1) d\eta d\zeta, \quad (36)$$

so that the integral in Eq. (6) may be evaluated as

$$\bar{Q} = \frac{\sum_{i=1}^N w_i Q(nf)_i |J|}{\sum_{i=1}^N w_i (nf)_i |J|}, \quad (37)$$

where the summations are over all the v -space sampling points in the discretisation, w_i is the weighting associated with the point, and $|J| = \pi r_v^2 (\eta_i + 1)/4$.

2.7. Parallelisation

Due to the large memory requirement involved in discretising both p -space and v -space domains, parallelisation of the algorithm is an essential requirement for the code to be applied to realistic problems. The code has therefore been parallelised using p -space domain decomposition to allow more significant problems to be tackled in a reasonable timeframe. The parallelisation procedure involved a master–slave setup and the following speedup plot is based on the number of slave processors running. With reference to Fig. 11, note that a superlinear speedup is achieved for up to 7 slave processors at which point the speedup tails off. This could presumably be improved by parallelisation of both v -space and p -space but an attempt at achieving this was deemed to be beyond the scope of the current work.

3. Results

3.1. The gas expansion problem

A highly rarefied gas of finite initial extent ($-L < x < L$) was modelled expanding into an infinite vacuum. This problem has a well defined analytical solution [1] and was therefore deemed a good test problem for the algorithm. A physical space mesh (see Fig. 12) with 1538 elements (4614 discontinuous nodes) combined with a velocity space mesh with 900 elements (961

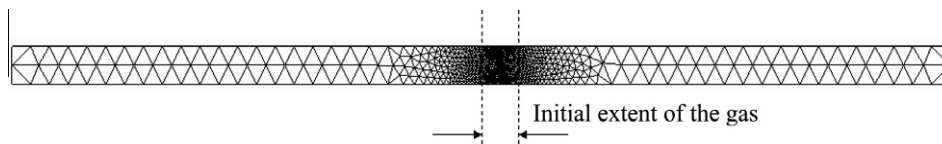


Fig. 12. Physical space mesh for gas expansion problem, Ω_r .

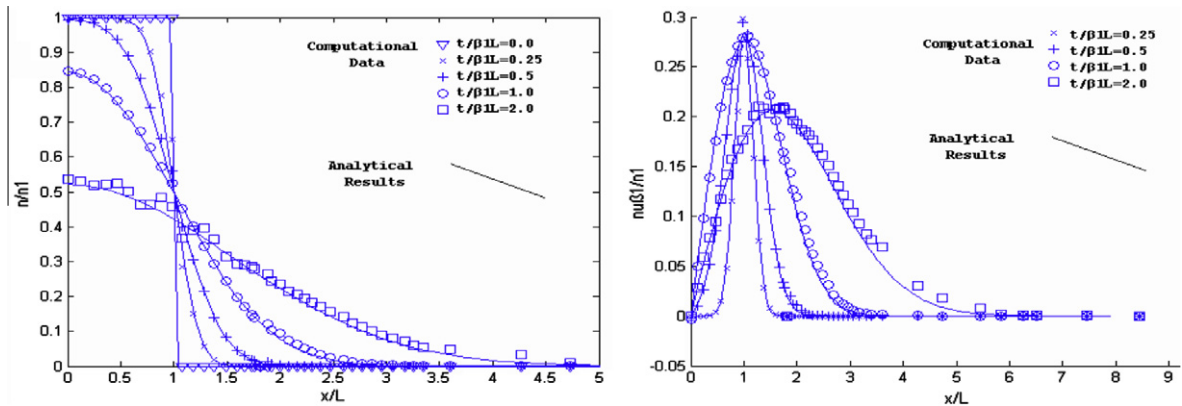


Fig. 13. Results for the gas expansion problem.

nodes) were used giving a total of 4,434,054 degrees of freedom. The simulation was run up to a non-dimensional time, $t/(\beta_1 L) = 8.0$, where $\beta_1 = \sqrt{1/(2RT_1)}$ with the Boltzmann equation RHS collision term switched off.

In the left-hand plot in Fig. 13, the time evolution of the non-dimensionalised number density is shown on the y-axis against the non-dimensionalised distance from the vertical centreline of the domain. In the right-hand plot in Fig. 13, the time evolution of a non-dimensionalised measure of momentum flux is shown on the y-axis against the non-dimensionalised distance from the vertical centreline. The solid lines show the analytical solutions and the various markers are data points from the computational mesh. It is clear that a good agreement between the solver data and the analytical solution to this problem has been achieved.

3.2. Flow over a vertical plate

The monatomic gas, argon, was modelled with the flow conditions at infinity set as $u = 172$ m/s, $T = 300$ K with corresponding Mach number $M = 0.53$ at a variety of Knudsen numbers. Fully specular reflection was the assumed boundary condition on the lower surface and on the vertical plate. This is analogous to a no-slip condition in the boundary condition of the macroscopic equations.

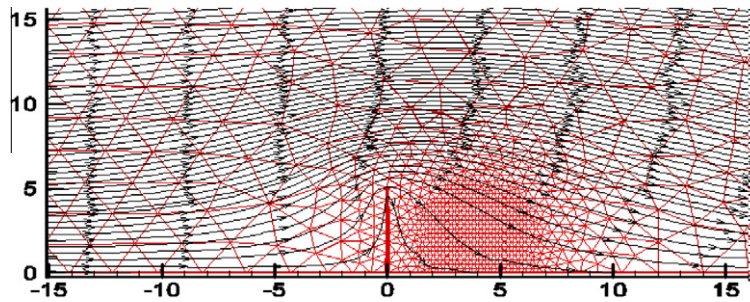
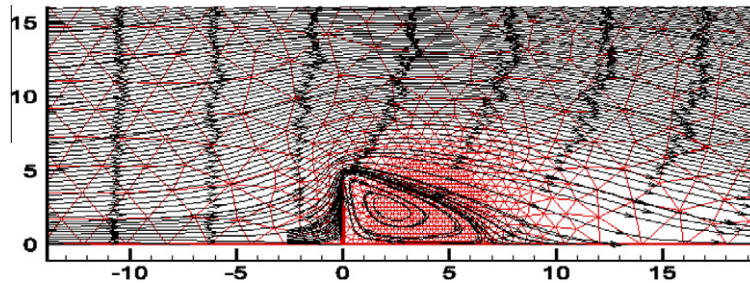
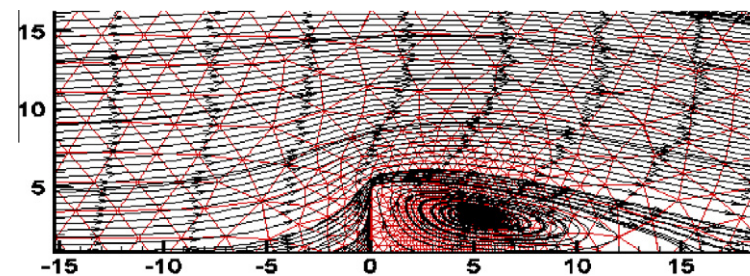
The p -space mesh used for these examples consisted of 2163 elements/6489 discontinuous nodes and was refined in the region downstream of the plate, where a vortex formation was expected. The v -space discretisation consisted of 400 sampling points with $r_v = 2000$ m/s. The runtimes to steady-state for these examples using the BGK code were several hours using 4 processors on the Swansea University C2EC PC Cluster.

We see from Figs. 14–16 that as the Knudsen number reduces, the downstream vortices produced by separation at the top of the plate become more significant features. This reduction in Knudsen number takes the problem from the free molecule regime, through the transition regime and to the fully continuous or Navier–Stokes regime. At large Knudsen number, molecular collision effects are small and, essentially, molecules travel in straight lines. It is, therefore, impossible for vortices to form. Reducing Kn by an order of magnitude from 1.0 results in a small, low velocity vortex and a further reduction in the order of magnitude of Kn results in a larger and higher velocity vortex. These results agree well with the same examples modelled by Bird [1] using a DSMC approach.

3.3. Rarefied hypersonic flow over a double ellipse

During the early stages of re-entry, a space vehicle will travel at extremely high velocity through a highly rarefied atmosphere [14]. The high Knudsen number ($Kn \gg 1$) of this flow allows it to be analysed using the collisionless Boltzmann equation.

A simple double ellipse geometry is used to model the nose region of a generic vehicle in two dimensions. Since these high Knudsen number runs assume a negligible effect due to molecular collisions, no shock will form and the solution will extend, in principle, infinitely far both upstream and downstream. The p -space mesh used for runs at a range of angles of

Fig. 14. Vertical plate $Kn = 1.0$.Fig. 15. Vertical plate $Kn = 0.1$.Fig. 16. Vertical plate $Kn = 0.01$.

attack from 40° to 20° is shown in Fig. 17. It consists of 7,565 elements/22,695 discontinuous nodes. Due to the extreme high velocities present in such a flow, the extent of the v -space domain had to be increased. By (numerical) experiment, it was determined that setting $r_v = 13,000$ m/s was sufficient. The number of sampling points in v -space was also increased from 400 to 1,000. This results in a value of 22,659,000 for the total number of degrees of freedom of the system. The positioning of the v -space sampling points is shown in Fig. 18.

In each of the three cases, the number density and Mach number distributions, constant pressure contours and streamtraces are shown. Each plot has been rotated such that the free-stream flow is horizontal. It is first important to note that no shocks form despite the Mach number being greater than 1. This is because the formation of a shock wave is dependent on collisions between molecules which are insignificant at $Kn \gg 1$. The flow solution must, therefore, vary continuously from regions where $M > 1$ to regions where $M < 1$.

The plots in Fig. 19(a), Fig. 20(a), Fig. 21(a) clearly show an order of magnitude increase in the molecular number density on the nose of the vehicle. The exact position of this region and its extent is also clearly dependent on the angle of attack. The effect of the vehicle on the number density extends out into the upstream flow a distance of the same order of magnitude as the vehicle diameter.

Coupled with the number density increase on the nose, is a pressure increase, detailed in the plots of constant pressure contours (Figs. 19–21). It is this pressure increase that causes the vehicle to decelerate to a velocity at which it can configure for landing. Above the nose there appears to be ‘spokes’ in the pressure contour pattern and a ‘jaggedness’ in the contours upstream. Investigations discovered that the formation of the spokes and the non-smoothness in the contours is connected with the pattern of sampling points in the v -space discretisation, i.e. they are not real flow phenomena. Using the spectral v -space discretisation approach used for this work, it is impossible to completely remove this numerical phenomenon, but minimising the tangential distance between sampling points in the far field of the v -space domain appears to help.

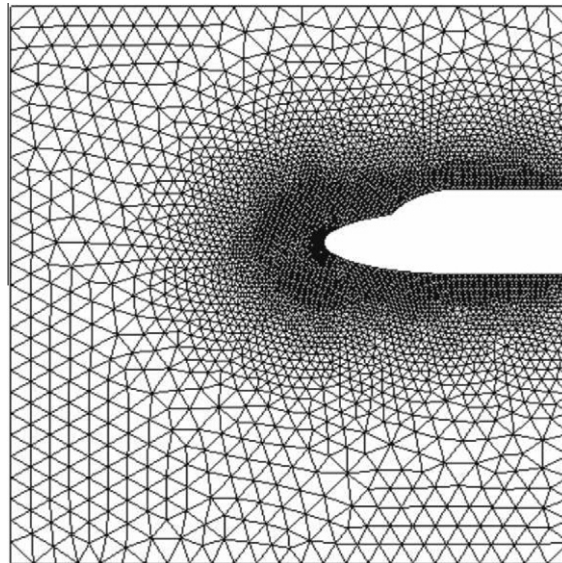


Fig. 17. Double ellipse mesh.

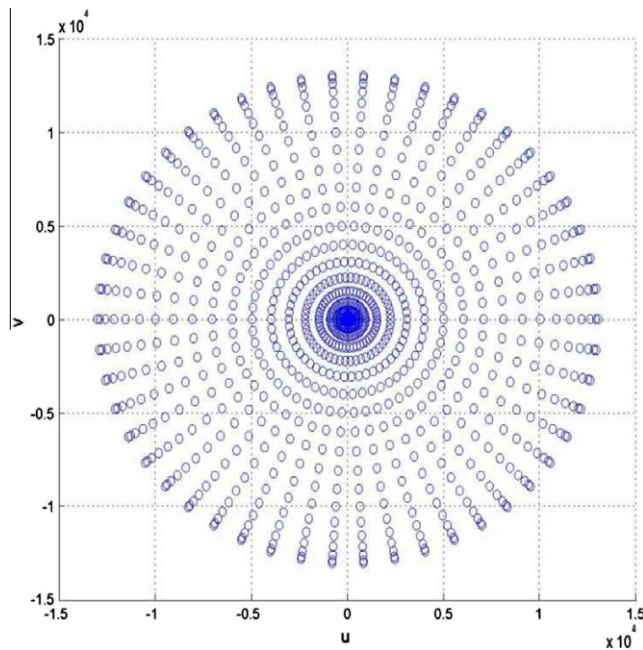


Fig. 18. V-space sampling points for the collisionless hypersonic examples.

This effect has also been noticed in neutron transport modelling using a discrete ordinate method [21]. This non-physical numerical phenomenon arises from the continuously varying angular nature of radiation being approximated by a specified set of discrete angular directions and is independent of the physical space discretisation. Remedies for the so called ray-effect have been suggested [22] and it is anticipated that future work will include the incorporation of one of more of these remedies to the solver presented here.

3.4. Flow over a NACA0012 Aerofoil

3.4.1. Transonic

Transonic flow over a NACA0012 aerofoil was examined next using the Boltzmann–BGK solver. Flow (of air) at a free-stream mach number, M_∞ of 0.85 and an angle of attack, AoA of 2° was considered at Reynold’s numbers, Re of 1,000 (case

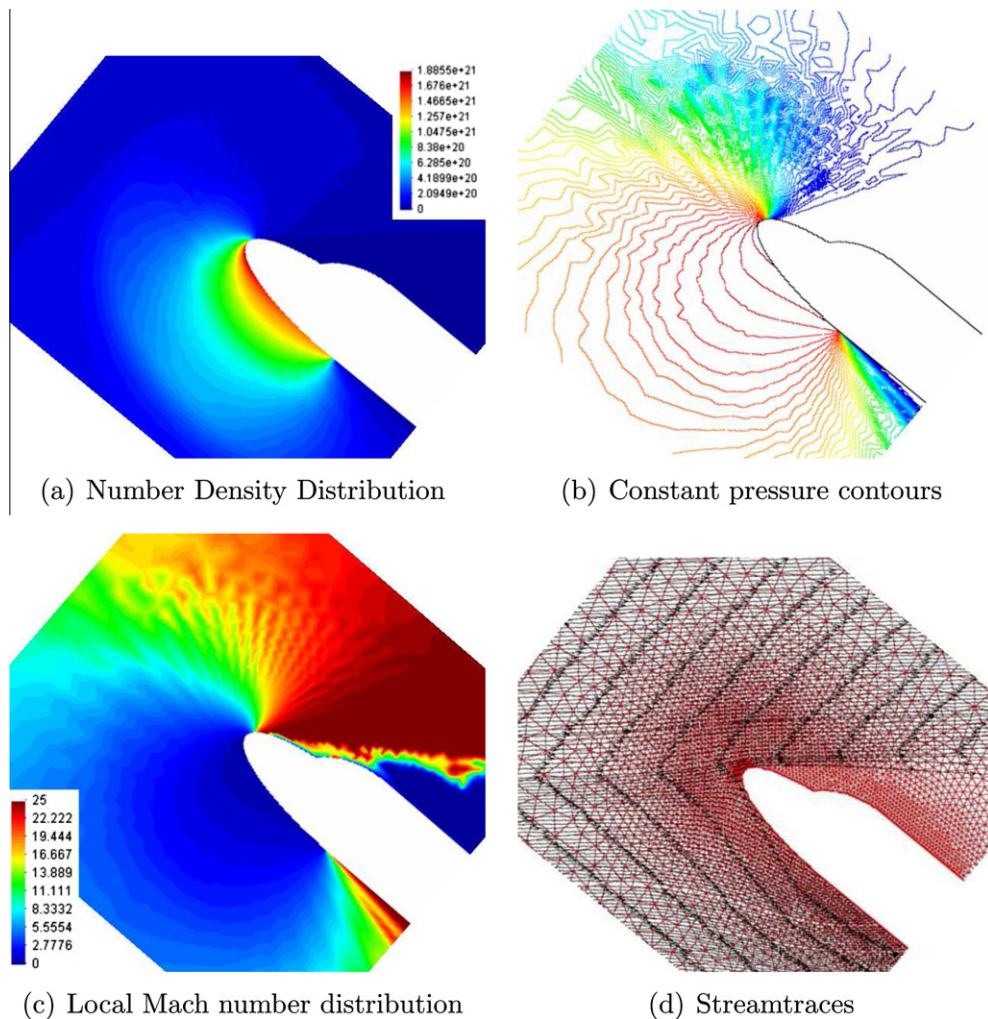


Fig. 19. Collisionless hypersonic case 1 ($M_\infty = 25, AoA = 40^\circ, Kn \approx 100$).

1) and 10,000 (case 2). These two cases correspond to flow with global Knudsen number, Kn_∞ (based on the aerofoil chord length) 0.002 and 0.0002 respectively. This places both cases well within the continuum regime and therefore could be solved using a traditional Navier–Stokes solver.

The initial P -space mesh used for these cases is shown in Fig. 22, consisting of 7640 elements/22920 discontinuous nodes. A region of mesh refinement is positioned around the aerofoil and downstream in an attempt to capture the boundary layer features, viscous wake and any shocks that may be present. The velocity space was discretised using 400 sampling points and $r_v = 2000$ m/s.

Fig. 23(a) and (b) show plots of constant pressure contours and constant Mach number contours for the case 1 steady-state solution. It is clear that the solution does not involve any shocks and a clearly defined downstream viscous wake is present. Also, the Mach contours indicate the presence of a thick boundary layer. These results compare well with data in the literature for NS solutions for the same flow conditions. The runtime to convergence using the Boltzmann–BGK solver was 14 h using 4 processors on the Swansea University PC Cluster. This is significantly longer than runtimes to convergence using a typical NS solver using similar computational resources.

In case 2, the Reynold's number, Re was increased by one order of magnitude with all other parameters held constant. The run was undertaken using the same mesh configuration as for case 1.

The pressure contour and Mach number plots for case 2 (Fig. 24(a) and (b)) indicate that increasing Re has resulted in the formation of a weak shock on the upper surface of the aerofoil. It is also evident that the boundary layer thickness has decreased. This is in agreement with an analytical analysis of the Prandtl equations for a flat plate boundary layer. This analytical analysis indicates that boundary layer thickness, δ is proportional to the square root of the inverse of Re ($\delta \propto \sqrt{\frac{1}{Re}}$). Again, a viscous wake region is present downstream of the aerofoil. Case 2 required a runtime to convergence of 70 h on 4 processors. This, again, is significantly longer than runtimes using a typical NS solver.

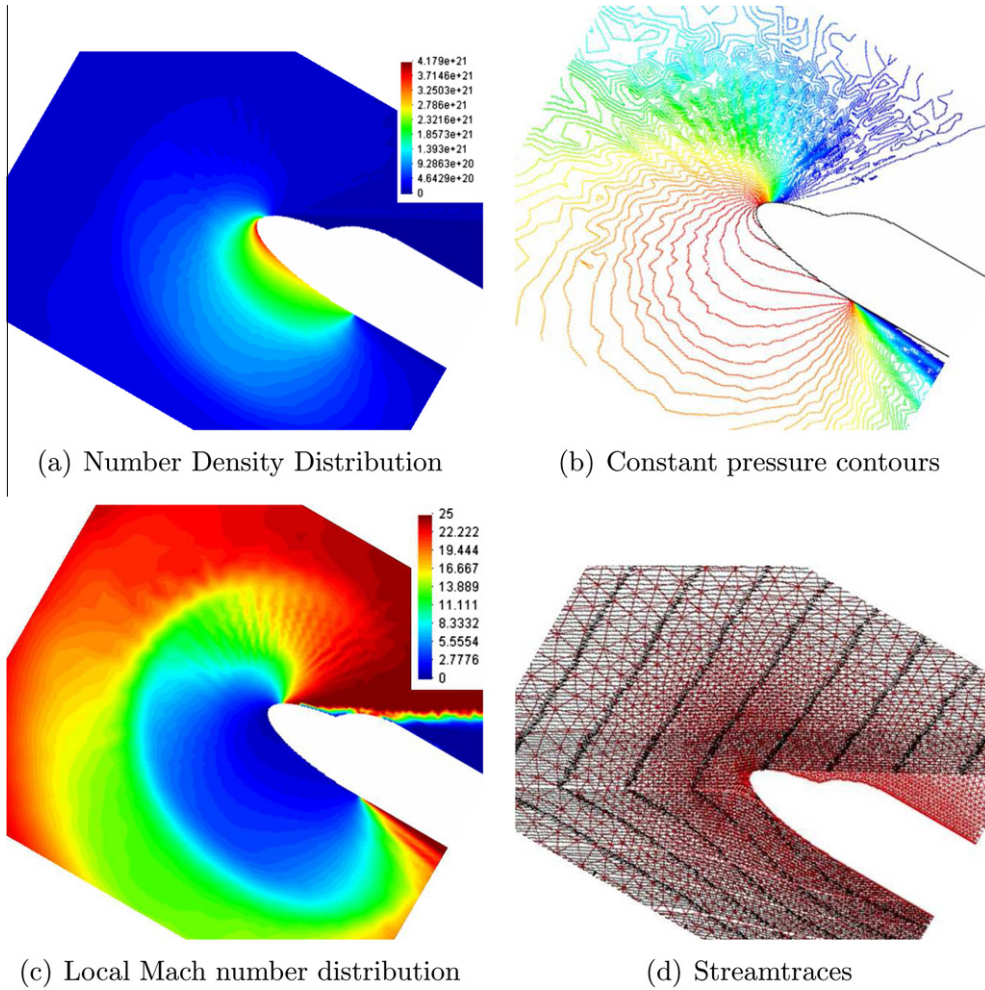


Fig. 20. Collisionless hypersonic case 2 ($M_\infty = 25, AoA = 30^\circ, Kn \approx 100$).

3.4.2. Supersonic

Finally, we examine supersonic flow over a NACA0012 aerofoil. The free stream Mach number, M_∞ was increased to 1.5 at $AoA = 0^\circ$ and $Re = 10,000$ ($Kn_\infty = 0.002$). The p -space mesh used was the same as that in the transonic cases (shown in Fig. 22) with 7640 elements/22920 discontinuous nodes. Again, v -space is discretised with 400 sampling points and $r_v = 2000$ m/s.

The pressure contour (Fig. 25(a) and Mach number contour (Fig. 25(b)) plots for the fully supersonic case indicate that the solution includes a weak detached bow shock with subsonic flow downstream. The shock has been smeared over a few elements (see Fig. 22). A crisper shock capture could be achieved by refining the mesh in the shock position indicated by this solution. The Mach number contour plot also indicates a viscous boundary layer and wake region. This wake region begins to get smeared in the far right of the plot in the region where element size increases (again, with reference to Fig. 22). This example clearly demonstrates the importance of using an appropriate mesh refinement to achieve an accurate solution. Both the pressure contour and Mach number plots agree well with Navier–Stokes solution for this flow (by, for example, Hafez and Wahba [25]). The streamtrace plot (Fig. 25(c)) shows no significant deflection of the flow at the bow shock which is to be expected for flow across a weak, approximately normal shock wave. The temperature distribution plot (Fig. 25(d)) does indicate a significant temperature increase across the shock. The temperature jump immediately across the shock is given by ($\frac{T_{downstream}}{T_\infty} \approx \frac{380}{294} = 1.29$). We can compare the Boltzmann–BGK estimation of the temperature jump with the isentropic normal shock relationship for a calorically perfect gas,

$$\frac{T_{downstream}}{T_\infty} = \frac{[2\gamma M^2 - (\gamma - 1)][(\gamma - 1)M^2 + 2]}{(\gamma + 1)^2 M^2} \tag{38}$$

This predicts a temperature jump of $\frac{T_{downstream}}{T_\infty} = 1.32$ which is a very good agreement and again, helps confirm that the Boltzmann–BGK solver is a suitable method for such flows. The temperature distribution plot also indicates significant viscous

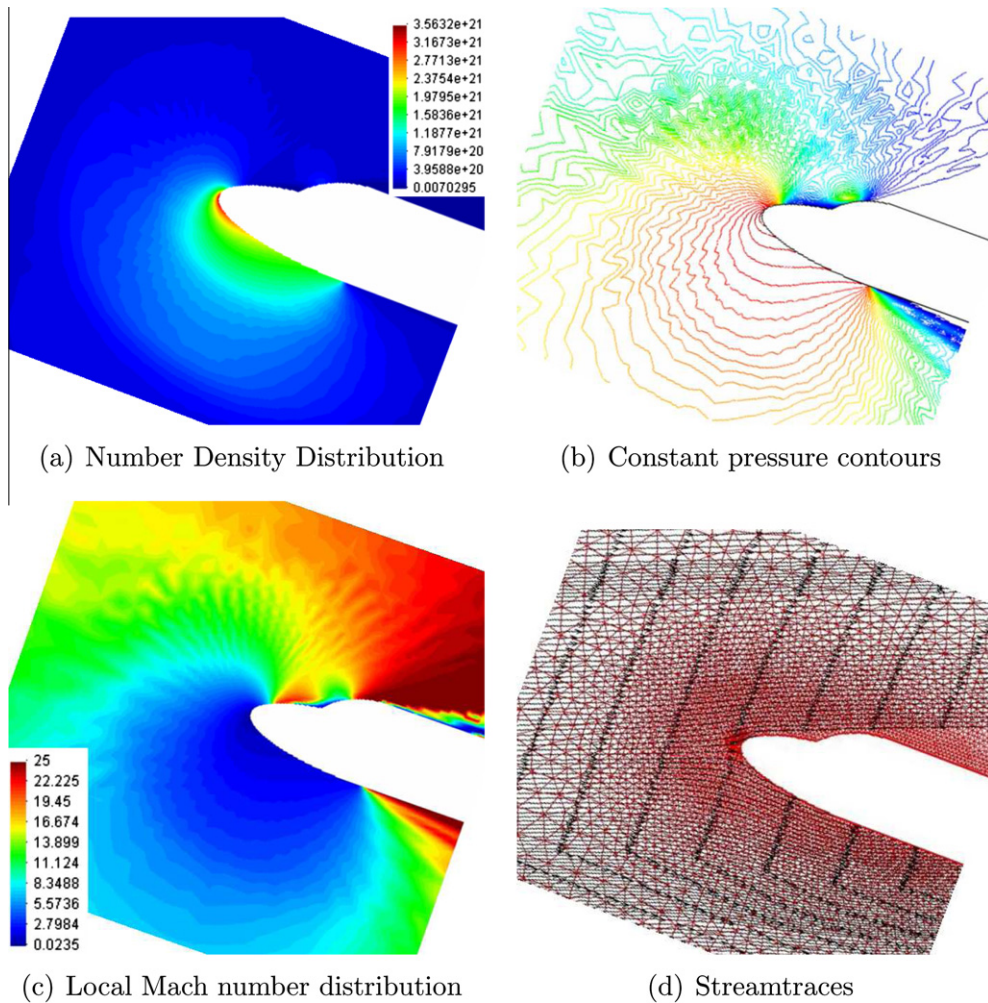


Fig. 21. Collisionless hypersonic case 3 ($M_\infty = 25, \text{AoA} = 20^\circ, Kn \approx 100$).

heating in the nose region and wake. The runtime to convergence was not competitive with typical NS solvers. For this example, a runtime of 40 h was necessary to achieve convergence on 4 processors.

4. Remarks

A finite element solver has been developed for the collisionless Boltzmann and Boltzmann–BGK kinetic equations of molecular gas dynamics. This is a very different approach to the standard approaches such as potential flow solvers, Euler solvers or NS solvers that have become the traditional, and popular tools of analysts in CFD. The Boltzmann–BGK solver, however, does not rely on the continuum assumption as do the other methodologies mentioned above. It considers the molecular behaviour directly and can, therefore, be applied to any flow, regardless of the degree of rarefaction, or the Knudsen number.

The finite element solver is of the two-step Taylor–Galerkin type. This is 2nd order accurate in both physical space and time. The elements used in physical space are linear, triangular and discontinuous. A spectral discretisation has been used in the velocity space domain for maximum efficiency.

The solver has been used to analyse a range of flow problems covering a broad spectrum of Knudsen number. The first example examined is a shock tube problem at high Knudsen number. The results shown agree well with analytical solutions. Next, subsonic flow over a vertical plate was analysed over a range of Knudsen number through the transition regime and into the continuum regime. We witness a good agreement with results from Bird’s DSMC model. A further high Knudsen number and high Mach number case was studied also studied; hypersonic flow over a double ellipse. Finally, transonic and supersonic flow over a NACA0012 aerofoil is analysed. These flows fall well within the continuum flow regime and the solutions agree well with results from standard NS solvers.

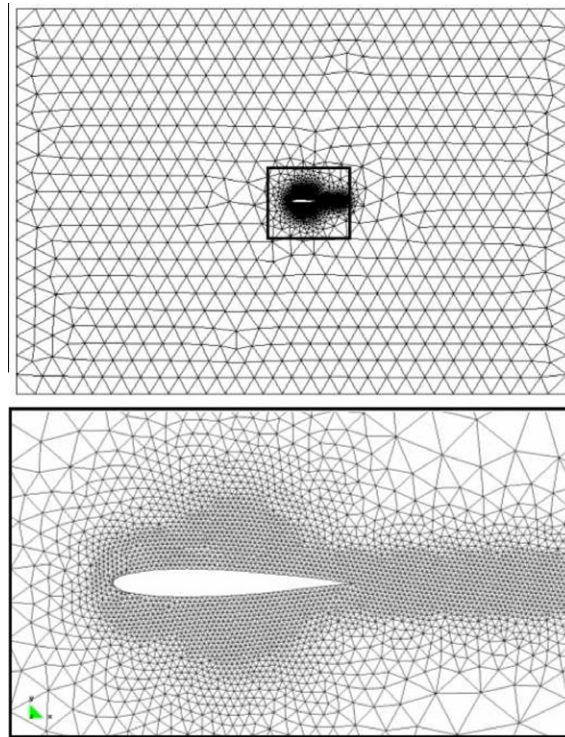


Fig. 22. p -Space mesh for NACA0012 aerofoil examples.

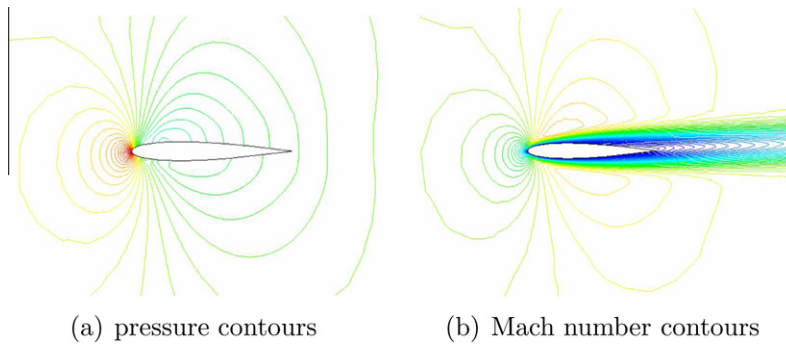


Fig. 23. Transonic case 1 ($M_\infty = 0.85, AoA = 2^\circ, Re = 1000$).

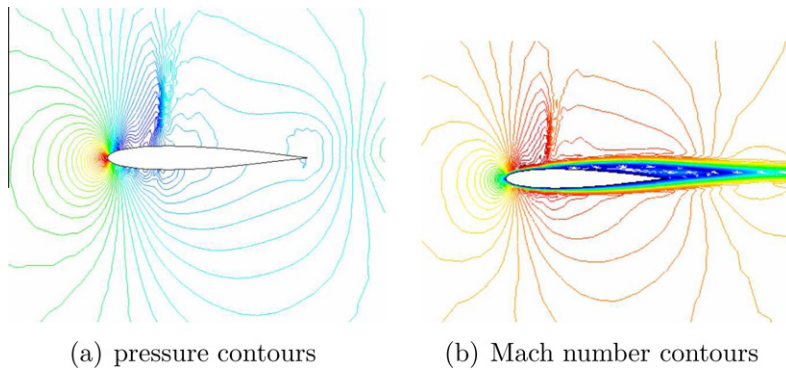


Fig. 24. Transonic case 2 ($M_\infty = 0.85, AoA = 2^\circ, Re = 10,000$).

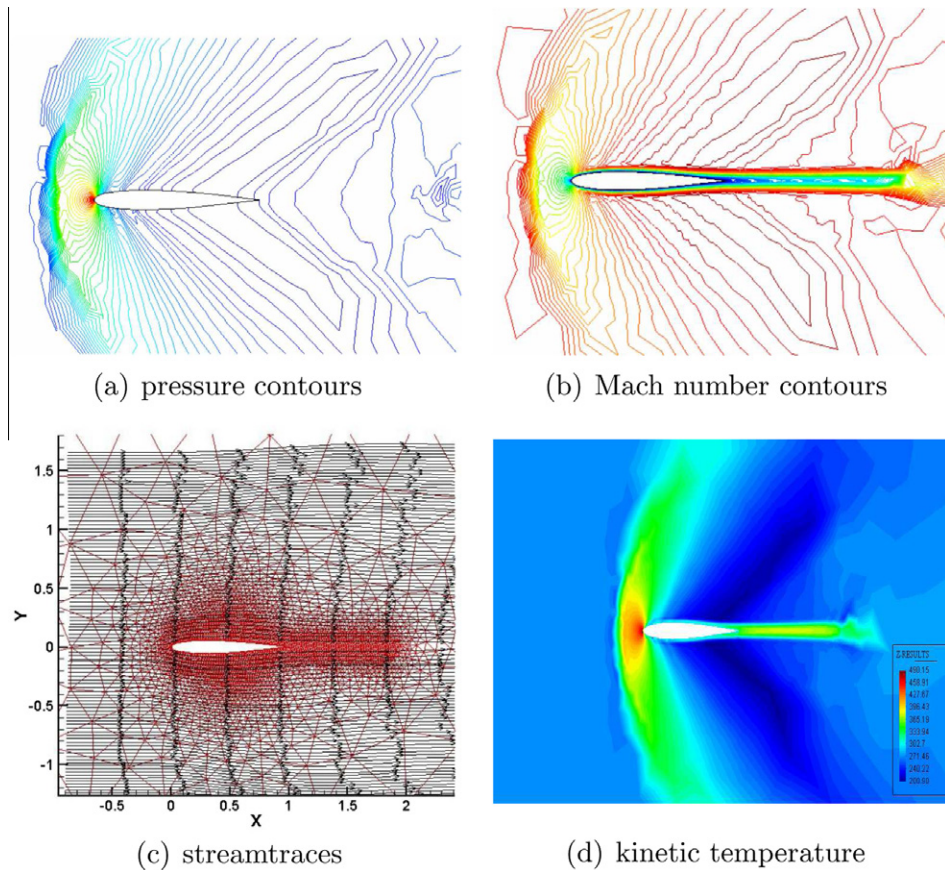


Fig. 25. Supersonic case ($M_\infty = 1.5, \text{AoA} = 0^\circ, \text{Re} = 10,000$).

Nonetheless, it is clear that the method presented in this paper is significantly more expensive computationally than the standard CFD techniques. A solution approach based directly on the Boltzmann–BGK equation is, therefore, only recommended for flows that feature truly non-equilibrium phenomena or have a Knudsen number that place them outside of the continuum regime.

Further development of the solver for the full Boltzmann equation will be attempted in future work and results compared with the Boltzmann–BGK approximation. Application to rarefied, hypersonic flow will also be attempted in which the non-equilibrium phenomena associated with the rarefaction and strong shocks are significant features. It may also be beneficial to attempt ‘patching’ the Boltzmann equation solver to a traditional NS solver, so that the more expensive Boltzmann algorithm is only applied in non-equilibrium zones.

References

- [1] G.A. Bird, *Molecular Gas Dynamics and the Direct Simulation of Gas Flows*, Oxford Science Publications, 1994.
- [2] N. Belleo, P. LeTallec, B. Perthame, Nonlinear Boltzmann equation solutions and applications to fluid dynamics, *App. Mech. Rev.* 48 (12) (1995).
- [3] H. Grad, *Encyclopaedia of Physics*, vol. XII, Springer-Verlag, Berlin, 1958.
- [4] C. Cercignani, *Mathematical Methods in Kinetic Theory*, Plenum Press, New York, 1969.
- [5] S. Harris, *An Introduction to the Theory of the Boltzmann Equation*, Holt, Rinehart, and Winston, New York, 1971.
- [6] J.C. Maxwell, On the dynamic theory of gases, *Phil. Trans. Soc.* 157 (49) (1867).
- [7] P.L. Bhatnagar, E.P. Gross, M. Krook, Model for collision processes in gases, I Small amplitude processes in charged and neutral one-component systems, *Phys. Rev.* 94 (1954) 511–524.
- [8] B. Cockburn, Discontinuous Galerkin methods, *J. App. Math. Mech.* 83 (11) (2002).
- [9] J. Donea, A Taylor–Galerkin method for convective transport, *Int. J. Numer. Meth. Fluids.* 20 (1984) 101–120.
- [10] L. Pareschi, S. Trazzi, Numerical solution of the Boltzmann equation by time relaxed Monte Carlo (TRMC) methods, *Int. J. Num. Meth. Fluids* 48 (2005) 947–983.
- [11] L. Darius, P. Gonzalez-Vera, F. Marcellan, Gaussian quadrature formulae on the unit circle, *J. Comput. Appl. Math.* 140 (2002) 159–183.
- [12] L. Trefethen, *Spectral Methods in MATLAB*, Society for Industrial and Applied Mathematics, Philadelphia, PA, 2000.
- [13] J.C. Maxwell, *Phil. Trans. Roy. Soc.* 1, Appendix, 1879.
- [14] F.J. Regan, *Dynamics of atmospheric re-entry*, AIAA Education Series, American Institute of Aeronautics and Astronautics, Inc., New York, 1993.
- [15] K. Morgan, J. Peraire, Unstructured grid finite-element methods for fluid mechanics, *Rep. Prog. Phys.* 61 (1998) 569–638.
- [16] J.T. Batina, Unsteady Euler airfoil solutions using unstructured dynamic meshes, in: *AIAA paper 89-0115*, AIAA 27th aerospace meeting, 1989.

- [17] O. Hassan, K. Sorensen, K. Morgan, N.P. Weatherill, Unsteady flow simulation using unstructured meshes, *Comput. Methods Appl. Mech. Eng.* 189 (2000) 1247–1275.
- [18] S. Chapman, T.G. Cowling, *The Mathematical Theory of Non-Uniform Gases*, second ed., Cambridge University Press, 1952.
- [19] C. Cercignani, *Theory and Application of the Boltzmann Equation*, Springer, 1988.
- [20] G. Busoni, A. Palczewski, A stationary Boltzmann equation near equilibrium, *C³AS: Math Models Methods Appl. Sci.* 3 (1993) 395–440.
- [21] C. John, A. Chai, S. Haek, B. Lee, V. Suhas, A. Patankar, Ray effect and false scattering in the discrete ordinates method, *Numer. Heat Transfer, Part B: Fundam.* 24 (4) (1993) 373–389.
- [22] K.D. Lathrop, Remedies for ray effects, *Nucl. Sci. Eng.* 55 (1971) 255–268.
- [23] D. Lefebvre, J. Peraire, K. Morgan, Finite element least squares solution of the Euler equations using linear and quadratic approximations, *Int. J. Comput. Fluid Dynam.* 1 (1993) 1–23.
- [24] O.C. Zienkiewicz, R.L. Taylor, *The Finite Element Method*, fourth ed., McGraw-Hill, Maidenhead, 1991. vol. 1.
- [25] M. Hafez, E. Wahba, Simulations of viscous transonic flows over lifting airfoils and wings, *Comput. Fluids* 36 (2007) 39–52.